

Fakultät für Mathematik, Informatik und Naturwissenschaften
Lehr- und Forschungsgebiet Informatik VIII
Computer Vision
Prof. Dr. Bastian Leibe

Seminar Report

Combining 3D Shape, Color, and Motion for Robust Anytime Tracking

Frederik Zwillling
Matriculation Number: 304314

June 2015

Advisor: Aljoša Ošep

Contents

| | | |
|----------|---|-----------|
| 1 | Introduction | 3 |
| 1.1 | Motivation | 3 |
| 1.2 | Tracking | 3 |
| 1.3 | Velocity and Pose Estimation | 4 |
| 2 | Related Work | 5 |
| 2.1 | Position and velocity estimation alternatives | 5 |
| 2.2 | Alternative Sensors | 6 |
| 2.3 | Grid-Based Methods | 6 |
| 3 | Method | 6 |
| 3.1 | Probabilistic Model | 6 |
| 3.2 | Adding Color and Motion | 9 |
| 3.2.1 | Motion Model | 9 |
| 3.2.2 | Color Model | 10 |
| 3.3 | Annealed Dynamic Histograms | 11 |
| 3.3.1 | Dynamical Refinement | 11 |
| 3.3.2 | Annealing | 13 |
| 3.3.3 | Resulting Tracking Estimate | 13 |
| 4 | Evaluation | 13 |
| 4.1 | Relative Reference Frame | 14 |
| 4.2 | Model Crispness | 16 |
| 5 | Conclusion | 16 |

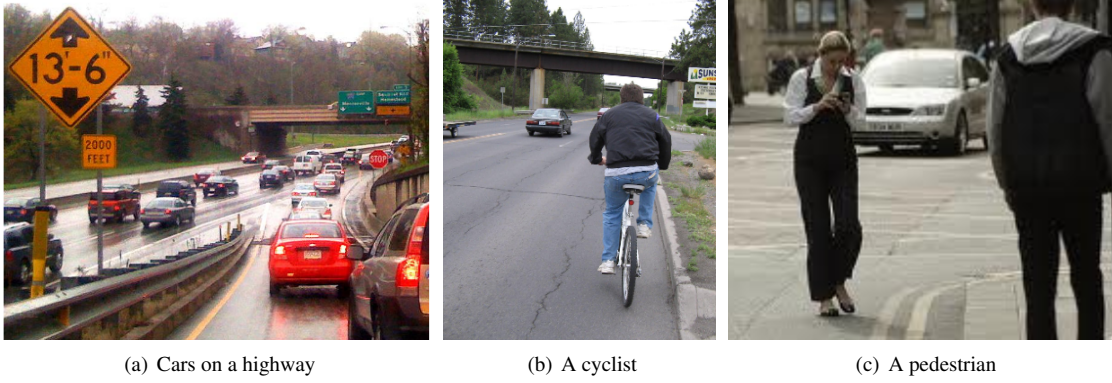


Figure 1: Various objects that have to be tracked in challenging situations [HLTS15]

1 Introduction

Robust and precise position and velocity estimation is an important part of object tracking. For example, it is an essential part in the collision avoidance of an autonomous car. This report presents a method by Held, Levinson, Thrun, and Savarese to solve this part of the tracking problem by combining clues of the 3D shape, color and motion of the tracked object [HLTS14]. The method uses a probabilistic measurement model derived from a Dynamic Bayesian Network. The search space, consisting of position and velocity, for each tracked object is represented in a special dynamic histogram, called *annealed dynamic histogram*. This histogram dynamically increases its resolution in the important areas and considers the local resolution in the measurement model. By expanding the measurement model with color and motion the performance of the method can be further improved. This is shown by the authors by evaluating in a static environment, where only the reference system is moving, and in a dynamic environment, where the compactness of the models build with the tracking results is used as evaluation criteria.

1.1 Motivation

Robotic applications are about to change many domains from the ground up. Especially autonomous systems could take over dangerous, exhausting and unpopular tasks and thus allow humans to do more satisfying tasks instead. Additionally, autonomous systems can be more efficient and scalable than solving the tasks by hand. Some progressive domains with autonomous robots are flying drones, which can map areas [RAK⁺07] or deliver packages [Ack13], autonomous cars, which take care of driving [Mar10], logistic robots, which store and grab goods in warehouses [Gui08], and domestic service robots, which can support old people and clean at home [IRdSvdZ12]. All these domains have in common that the robots have to track objects in their environment, mostly for avoiding collisions. In the case of domestic service robots, tracking is also needed for follow people. Often the reliability and precision of the tracking are limiting factors. An autonomous car, for example, can only drive fast if it is sure that it tracks all objects in the surrounding correctly and none of these objects could cause a collision. This report mainly focuses on the domain of autonomous cars. Here, the autonomous system takes care of the time consuming driving task on the one hand and could help to reduce the amount of traffic deaths (25,938 in 2013 in the EU [Eur15]) on the other hand. In this domain it is especially important to estimate the speed of various nearby objects robustly and in real time. Figure 1 shows the three main classes of objects that have to be tracked, cars, bicycles, and pedestrians, in challenging situations. The method proposed in this report solves this task and performs better than previous approaches in the car domain.

1.2 Tracking

Object tracking is the complex task to identify objects and their movement over time. It can be separated into the following parts. The first step segments the sensor data for time t , called *frame*, into detected objects. This can be done for example by separating foreground and background and find connected components

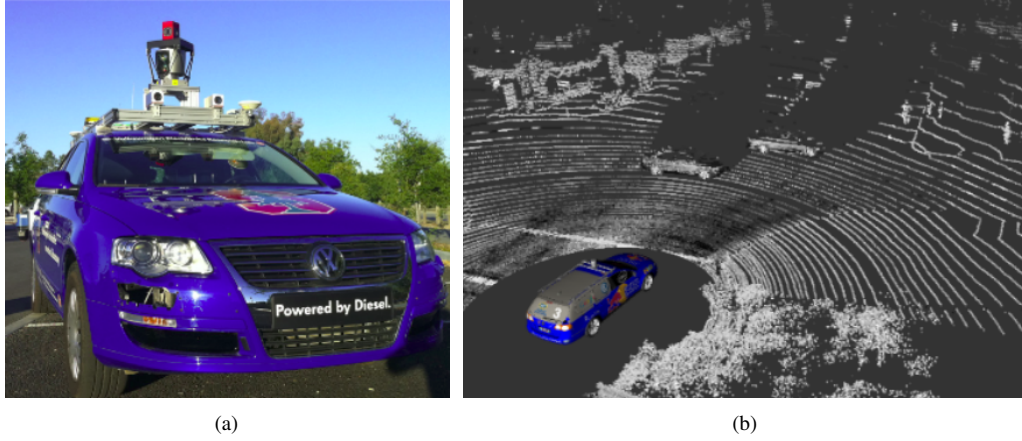


Figure 2: A Velodyne LIDAR sensor mounted on a car (a) and a visualization of the point cloud generated by it (b) [TLT11].

in the foreground. In this step, it is beneficial to use the information that the most important objects to find are cars, bicycles and pedestrians [WPN12]. The second step is to associate detected object in the successive frames t and $t + 1$. One method to find these matchings is to compute descriptors, such as the HOG descriptor, for the objects and find nearest neighbors in the descriptor space [TLT11]. The third step is the position and velocity estimation of the tracked object. That is the part of tracking this report is about. In the fourth step, the computed trajectory of the tracked object is classified to decide, for example, if the object is dangerous to the car.

The data that is used for tracking in this report is generated by a dense laser sensor that measures the distance to surrounding objects with multiple rotating laser beams. Such a sensor and the data generated by it is shown in Figure 2. Additionally, the sensor provides a camera image similar to a panorama.

1.3 Velocity and Pose Estimation

To compute the pose and velocity estimation of an object, we first introduce a measurement model that is derived from a Dynamic Bayesian Network (*DBN*). This *DBN* models for each frame the dependencies between position, velocity, object surface and the observed measurement as well as the dependencies between two frames. Though, tracking is a hard problem because in cases with occlusion and major changes in the viewpoint the visible object surface can differ significantly and introduce an error. Especially in these cases, it is intuitive to also consider color and motion in the measurement model because the additional information is influenced less by occlusion and viewpoint changes.

To find the state, which is composed of position and velocity of an object, we use a histogram that maps the each histogram-chunk in the state space to the probability that this chunk causes the measurement according to our model. This allows a global search in the state space with multiple hypothesis. A standard histogram with adequate resolution would have to many chunks and thus would be too slow for real time computation. Therefore, we use a dynamic histogram that starts with a low resolution and an approximated posterior distribution. Then it dynamically increases the resolution in areas with high probability to cause the measurement. This allows to achieve a result after running the method for any time. The downside of the dynamic histogram is that the initial low resolution introduces an additional error. This can be balanced by including the resolution in the measurement model. We call this method *annealed dynamic histogram* because as the resolution increases, the distribution is annealed and approaches the true posterior.

The evaluation in Section 4 shows that the method outperforms other tracking methods by about 10%.
 Maybe add more evaluation intro?

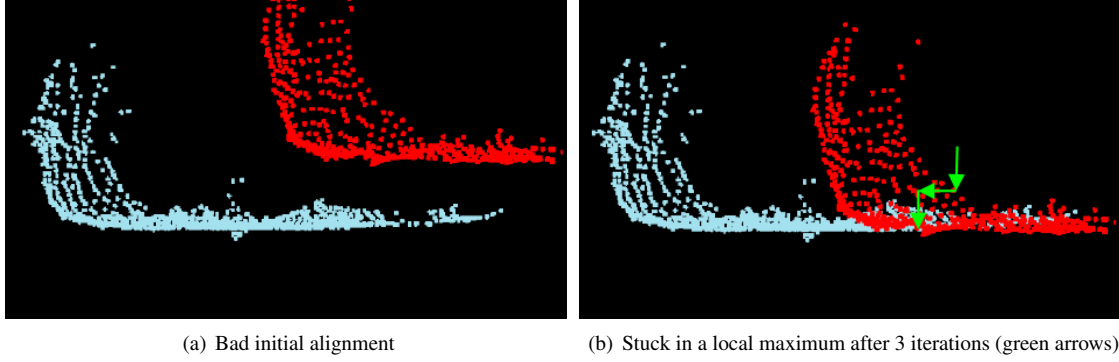


Figure 3: Possible case for bad ICP alignment results. The two point clouds belong a detected car in successive frames [HLTS15].

2 Related Work

The tracking problem has been studied for many years. The most common approaches to estimate the position and velocity of tracked objects, namely Kalman filters and Iterative Closest Point, are described in subsection 2.1. Often these approaches are efficient but sacrifice a lot of the available data by using simple representations or search only for a local maximum. Because our case of tracking objects in 3D point clouds from a laser sensor is only a special case of tracking, subsection 2.2 gives an overview of the tracking approaches with other sensors, mainly single cameras and stereo cameras. Subsection 2.3 presents grid-based approaches that are similar to annealed dynamic histograms.

2.1 Position and velocity estimation alternatives

Some simple approaches to estimate position and velocity of a tracked object first represent the object by its centroid [KMPS12, LAB⁺11] or bounding box [AA12, LHT⁺08, SFD02] and then use a Kalman filter [RN13]. This is a computationally efficient approach but discards a lot of available information by using such a simple representation. Therefore, this approach is especially fragile in cases of occlusion and viewpoint changes. In the occlusion case, the bounding box can contain only a part of the object and the centroid would be shifted. In the viewpoint-change case, the centroid and bounding box can significantly differ (e.g. when seeing a cyclist from the back and the side). Another disadvantage of the Kalman filter is that it can only represent a single hypothesis and thus performs poorly when multiple hypotheses are reasonable.

Other approaches include domain specific knowledge to use better fitting object representations. For example, the typical shape of a car with its corners or wheels can be used to achieve a more precise position of a car in a frame [WH12, DRU08, PT09]. This leads to better detection and association results, but is limited by the amount of trained object-classes. Although cars, pedestrians and cyclists are the most common classes, it is also important to detect uncommon obstacles in traffic (e.g. tractors, segways, and wheelchairs). The work presented in this report is based on [TLT11]. It allows recognition and classification of arbitrary objects and only requires labeled dataset to train the object-classes. Another approach that can track known objects as well as fully unknown objects is [ML12]. This approach differs from the previous ones by performing the tracking before the detection step what enables it to track unknown objects.

A widely used alternative to Kalman filters is the Iterative Closest Point (ICP) algorithm [FHB12, MS13, ML12]. The algorithm merges two point clouds by finding a maximum correspondence alignment. Thus the full 3D point cloud is used. It uses a hill climbing approach and therefore depends on a good initialization and can get stuck in a local maximum. This is the major drawback of ICP and has a large impact on the tracking precision as shown by [HLT13, Ols09]. Figure 3 visualizes how ICP can return a wrong alignment after an unlucky initialization. The approach presented in this report performs a global search and therefore has no problem with local maxima.

2.2 Alternative Sensors

Laser range sensors, such as the one shown in Figure 2, are not the only kind of sensors used for tracking tasks. Although laser range sensors provide more precise data compared to other sensors used for tracking, they are inadequate for many applications because of their high price. A closely related alternative to laser range sensors is the usage of stereo cameras. They provide the same kind of data (point clouds and images) and are cheap. However, they have more noise than a laser sensor and can therefore cause larger errors in the tracking results. An example for the use of stereo data for tracking is [ML12]. It uses ICP to track pedestrians and unknown objects. Object tracking with a single camera has been studied for a long time and is used in many applications, e.g. in video calling [KH95]. However, single camera tracking is unsuitable in the autonomous car scenario because of missing depth information.

2.3 Grid-Based Methods

Ordinary grid-based search approaches in computer vision are used to globally search in a state space and allow multiple hypothesis in contrast to Kalman filters and ICP. However, the computational effort increases with the resolution of the grid. Therefore, ordinary histograms are often inadequate for domains which require real time computation. Dynamic histograms tackle this problem by starting with a low resolution and increasing the resolution in important areas. However, this creates the problem that the low resolution introduces an additional error.

There already are some grid-based approaches which tackle this problem. Most of them are used in Simultaneous Localization and Mapping (*SLAM*). [ECM04] uses a grid-based Monte-Carlo method that recursively expands grid cells with the most hypotheses and refines the grid resolution in these cells. This only differs from annealed dynamic histograms in the usage of a Monte-Carlo distribution instead of probabilities to cause the current measurement. The approach presented in [MSM02] self-localizes a robot with a dynamically refined grid. Here, each measurement point votes for the cells that could have caused the measurement. The cells with the most votes are refined in the next iteration. Similarly to the paper presented in this report, the approach enables anytime computation.

The main differences between previous methods and the method presented in this report are the additional consideration of color, what is not directly possible in Kalman filter or ICP approaches, and the consideration of the probabilities for points being occluded in previous frames. This leads to higher tracking robustness. Furthermore, annealed dynamic histograms allow multiple hypotheses and globally searching the state space. In contrast to other grid-based approaches, it also allows real-time computation without introducing a high error resulting from low resolution by annealing the measurement model as the resolution increases.

3 Method

The method presented in this report consists of three major parts. Subsection 3.1 introduces the probabilistic model based on a Dynamic Bayesian Network. The model is necessary to determine how likely it is that a specific position and velocity of a detected object causes the observed measurement. In Subsection 3.2 the extension of the measurement model by color and motion is shown [HLTS14]. Subsection 3.3 describes how annealed dynamic histograms are used to search the state space for the most likely position and velocity according to the measurement model. For that especially the refinement steps, that increase the resolution, and the annealing of the measurement model depending on the resolution are important.

3.1 Probabilistic Model

To derive the probability for a position and velocity to cause the observed measurement seen in the last frames, we use a Bayesian Network because it allows us to easily combine 3D shape, color, and motion cues [HLTS14]. After encoding the influences of the states, consisting of position and velocity, the surface of the object to track and the observed measurement, we can derive the wanted probability of the measurement given the state by applying well known probability rules in Bayesian Networks [RN13]. Furthermore, we use a Dynamic Bayesian Network to relate variables over successive time steps.

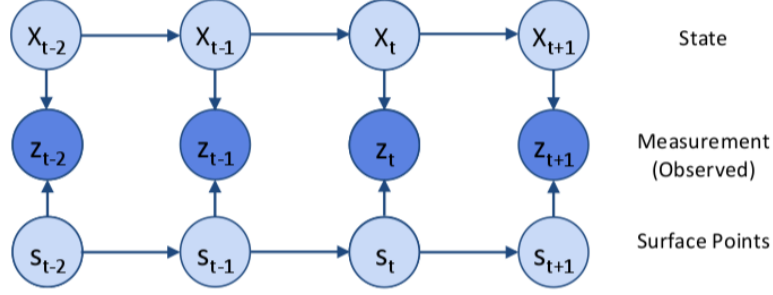


Figure 4: Dynamic Bayesian Network to derive the measurement model for tracking an object [HLTS14].

The Dynamic Bayesian Network we use to derive the measurement model is shown in Figure 4. For the frames $t-2$ to the current frame $t+1$, it includes the variables x for the state, z for the observed measurement and s for the visible surface of the object. In the following, we describe these variables in detail.

As state variable x_t , we use the composition of position and velocity $x_t = (x_{t,p}, \dot{x}_{t,p})$. $x_{t,p}$ is the linear position of the object centroid in frame t relative to the centroid of the object in frame $t-1$. In other words, the centroid of the object in frame $t-1$ is the origin of the coordinate system for $x_{t,p}$. $\dot{x}_{t,p}$ is the velocity of the object. The relative rotation and the rotational velocity of the object is not included in the state. This speeds up the method because a lower dimensional state space is considered. The authors claim that omitting the rotation is no problem because the rotational velocity of the objects present in traffic is small relative to the frame rate of the sensor, which is $10Hz$. Similarly, also the vertical movement of the objects is small because the objects we are interested in move along the ground. Therefore, we can use a 2D position and velocity instead of a 3D position and velocity. To use the methods in other domains that require considering the vertical velocity, the state space can be expanded, what results in a slow down of the method.

To include the 3D shape of the object in the model we use the latent surface variable s_t . It represents the visible surface of the object and is a set of n points $\{s_{t,1}, \dots, s_{t,n}\} = s_t$ that are sampled from the visible surface. Although the true 3D shape of the object is unknown and only indirectly observable through the measurement, it is important for the model. This is similar to SLAM methods which model the environment map that corresponds to the surface in our terminology. The measurement then depends on the modeled map and the localization, or the object surface and state in our case.

When looking at the Dynamic Bayesian Network in Figure 4, it is easy to see that considering the surface is important because, when it is omitted, two successive measurements would be independent given the state variable. This would be wrong because the shape of the object is relatively consistent and therefore also the measurement points describe a similar surface. In contrast to SLAM, it is not our goal to build the shape of the observed object. We simply integrate over shapes to get the surface. The prior of the surface points $p(s_{t,i})$ is a uniform distribution over the maximum size of an object. The prior of the surface is the product over its points $p(s_t) = \prod_i p(s_{t,i})$. The observed measurement z_t is again a set of measurement points $z_t = \{z_{t,1}, \dots, z_{t,m}\}$. These points depend on the latent surface s_t and the position $x_{t,p}$. However, the measurement points do not lie directly on the surface as illustrated in Figure 5. This is caused by the sensor noise, which depends on the sensor resolution and is modeled as Gaussian noise Σ_e . The sensor resolution can roughly be modeled as a linear function of the distance between

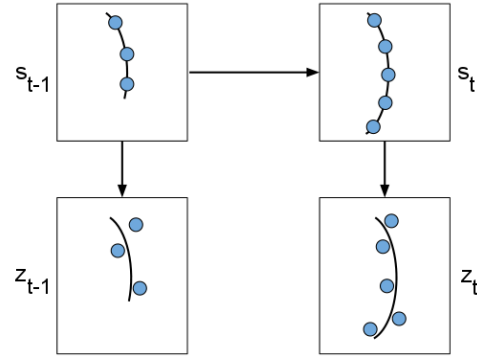


Figure 5: Measurement points z_t sampled with sensor noise Σ_e from surface points s_t . The visible surface, from which the surface points are sampled, varies from frame to frame due to occlusion and viewpoint changes [HLTS14].

object and sensor. The generation of measurement points z_t depending on the surface points s_t , the sensor noise Σ_e and the position $x_{t,p}$ can be written as

$$z_{t,i} \sim \mathcal{N}(s_{t,i}, \Sigma_e) + x_{t,p} . \quad (1)$$

Because the origin of the coordinate system is placed at the centroid of the object in the previous frame, the measurements of the previous frame are not shifted

$$z_{t-1,i} \sim \mathcal{N}(s_{t-1,i}, \Sigma_e) . \quad (2)$$

Therefore, z_{t-1} is conditionally independent from x_{t-1} what is not derivable by just using the Bayesian Network in Figure 4.

For the derivation of the measurement model, we will also need the term $p(s_t|s_{t-1})$ which stands for the probability of sampling surface points s_t from the currently visible surface given s_{t-1} from the previous frame. The sampled points might differ because of occlusions, viewpoint changes, random sampling from the surface and deformations of the object (e.g. body movement of a walking pedestrian). Every point of s_t could have been generated from a visible or occluded part of the surface in frame $t-1$. When we consider the prior probability $p(V)$ for sampling from a previously visible surface, we can use the joint distribution over these two cases:

$$p(s_{t,i}|s_{t-1}) = p(V) * p(s_{t,i}|s_{t-1}, V) + p(\neg V) * p(s_{t,i}|s_{t-1}, \neg V) \quad (3)$$

$p(s_{t,i}|s_{t-1}, \neg V)$ stands for the probability that $s_{t,i}$ is generated from a part of the surface that was not visible in the previous frame. Under the assumption that every non visible point is occluded, we can rewrite the term with constants k_1 and k_2 :

$$p(s_{t,i}|s_{t-1}, \neg V) = k_1(k_2 - p(s_{t,i}|s_{t-1}, V)) \quad (4)$$

This allows simplifying Equation 3 to

$$p(s_{t,i}|s_{t-1}) = \eta_1(p(s_{t,i}|s_{t-1}, V) + k) \quad (5)$$

with the normalization constant $\eta_1 = p(V) - p(\neg V)k_1$ and the smoothing factor $k = p(\neg V)k_1k_2/\eta_1$. These constants can later be found by training.

$p(s_{t,i}|s_{t-1}, V)$ can be modeled by a Gaussian distribution

$$s_{t,i} \sim \mathcal{N}(s_{t-1,j}, \Sigma_r) \quad (6)$$

where $s_{t-1,j}$ is the closest corresponding surface point from the previous frame and Σ_r is the variance mainly resulting from the sensor resolution and the object deformation. Combining these Gaussians in Equation 5 for all surface points in s_t yields

$$p(s_t|s_{t-1}) = \eta(\mathcal{N}(s_t; s_{t-1,i}, \Sigma_r) + k). \quad (7)$$

For the measurement model used in the annealed dynamic histogram, we need to derive $p(z_t|x_t, z_1, \dots, z_{t-1})$, the probability for the current measurement given the histogram cell with state x_t and the previous measurement history z_1 to z_{t-1} . Though considering all previous measurements of the object would be computationally costly. Although the measurements in different time frames are not independent given the state, as discussed earlier, we can focus only on the previous one as approximation, because the previous one has the highest impact of all measurements in the history.

$$p(z_t|x_t, z_1, \dots, z_{t-1}) \approx p(z_t|x_t, z_{t-1}) \quad (8)$$

This approximation can be rewritten by using the joint distribution over all surface points in the current and previous frame:

$$p(z_t|x_t, z_{t-1}) = \iint p(z_t, s_t, s_{t-1}|x_t, z_{t-1}) ds_t ds_{t-1} \quad (9)$$

Because of the chain rule of probabilities and the conditional independences that could be derived from the Dynamic Bayesian Network in Figure 4, we can refine the term in the integral:

$$\begin{aligned} p(z_t, s_t, s_{t-1} | x_t, z_{t-1}) &= p(z_t | s_t, x_t) p(s_t | s_{t-1}) p(s_{t-1} | x_t, z_{t-1}) \\ &\stackrel{(2)}{=} p(z_t | s_t, x_t) p(s_t | s_{t-1}) p(s_{t-1} | z_{t-1}) \\ &= p(z_t | s_t, x_t) p(s_t | s_{t-1}) \eta_2 p(z_{t-1} | s_{t-1}) p(s_{t-1}) \end{aligned} \quad (10)$$

η_2 is again a normalization constant and can be used to absorb the constant term $p(s_{t-1})$. This term is constant because it is the product of a constant number of uniformly distributed probabilities of the surface points. This allows simplifying the term in the integral further:

$$p(z_t, s_t, s_{t-1} | x_t, z_{t-1}) = \eta \underbrace{p(z_t | s_t, x_t)}_{(1)} \underbrace{p(s_t | s_{t-1})}_{(7)} \underbrace{p(z_{t-1} | s_{t-1})}_{(2)} \quad (11)$$

For this term, we have modeled all probabilities as Gaussians as indicated under Equation 11. Therefore, the term only consists of a product of Gaussians and Gaussians plus a constant. If we plug in Equation 11 back into our integrals in Equation 9, we can apply a convolution of Gaussians to solve the inner integral [TBF05]. Because the convolution of two Gaussians results in a Gaussian, we can apply a convolution of Gaussians again to evaluate the outer integral and yield a Gaussian for the measurement model:

$$p(z_t | x_t, z_{t-1}) = \eta (\mathcal{N}(z_t; z_{t-1} + x_{t,p}, \Sigma_r + 2\Sigma_e) + k) \quad (12)$$

For the computation of the measurement model, we introduce the variable $\bar{z}_{t-1} = z_{t-1} + x_{t,p}$ so that the measurement in the previous frame is shifted according to x_t . Then for each $z_{t,i} \in z_t$, we have to find the closest corresponding point $\text{ccp}(z_{t,i}) = \bar{z}_{t-1,j} \in \bar{z}_{t-1}$. The measurement probability for the current measurement given the inspected state and the previous measurement can be computed by

$$p(z_t | x_t, z_{t-1}) = \eta \left(\prod_{z_{t,i} \in z_t} \exp \left(-\frac{1}{2} (z_{t,i} - \text{ccp}(z_{t,i}))^T \Sigma^{-1} (z_{t,i} - \text{ccp}(z_{t,i})) \right) + k \right) \quad (13)$$

with normalization constant η , smoothing factor k , and covariance matrix $\Sigma = 2\Sigma_e + \Sigma_r$. Again these constants and the function for Σ_r , which depends on the distance between sensor and tracked object, can be found by optimizing for a set of training data.

The computation with Equation 13 works well if the point clouds z_t and z_{t-1} have a similar size. Because of occlusion the size of the point clouds can vary. This is a problem because Equation 13 is not symmetric with respect to z_t and z_{t-1} . For example when a part of the detected object becomes unoccluded in comparison to the previous frame, z_t is larger than z_{t-1} and therefore each point in z_t that has no nearby correspondence in z_{t-1} adds a large penalty. This would result in an incorrect alignment because the tracker would try to minimize the number of badly matchable points and therefore focuses on aligning the densest parts of the pointclouds. This problem can be solved by exchanging z_t and z_{t-1} so that always the smaller point cloud is aligned in the larger one. In the case of such an exchange, the implementation also has to consider the switch of the coordinate system origin.

3.2 Adding Color and Motion

So far, the measurement model considers the 3D shape of the object to tell us how likely it is that a state causes the measured point cloud. To increase the robustness and precision of the tracker, we also want to consider clues from motion and color. This especially improves the performance in comparison to ICP which only uses the object shape [HLTS14].

3.2.1 Motion Model

For the motion model, we use a constant velocity model of a Kalman filter [TBF05]. In each iteration, the Kalman filter algorithm is fed in the measurement step with a Gaussian that represents the probabilities for the states to cause the current measurement. Furthermore, in the motion step of each iteration the expected

motion of the object in the time till the last iteration is applied to the position of the object. Both steps are computed by combining two Gaussians. As a result, the algorithm gives a Gaussian for the position and motion of the object.

We just need to give the algorithm a Gaussian for the measurement step. For this we can use the results of the measurement model that have to be represented as a Gaussian. This can be done by computing the mean μ_t and variance Σ_t for all states weighted by the probability $p(x_t|z_1, \dots, z_t)$.

$$\begin{aligned}\mu_t &= \sum_i p(x_{t,i}|z_1, \dots, z_t) x_{t,i} \\ \Sigma_t &= \sum_i p(x_{t,i}|z_1, \dots, z_t) (x_{t,i} - \mu_t)(x_{t,i} - \mu_t)^T\end{aligned}$$

where $x_{t,i}$ is the state of sample i .

3.2.2 Color Model

The model we have developed up to this point considers the 3D shape and motion of tracked objects. As presented in the evaluation in Section 4, this model can be used to implement the tracker and yields reliable results. Although we also want to add color information to the model, this is important because color information is not always available (e.g. when the autonomous car is driving in the dark). To incorporate the fact, that the color of the surface points should match between two successive frames, into the model, we first need to learn the probability distribution of color matchings. This can be done by analyzing a dataset with already known alignments. For an autonomous car, such a dataset can be easily obtained by driving in a static environment (e.g. along a row of parked cars). The alignment of the tracked objects can then be computed with the speed of the car and the position of the tracked object relative to the car. For the analyzing of color matchings, then the nearest points of two subsequent measurements can be used. It is reasonable to use only the correspondence pairs with a distance under a certain threshold (5cm was used by the authors of the paper). Although it would be intuitive to use all available color channels, we use only the blue color channel. This simplifies the problem, because we do not need to learn the covariances between the color channels, and already increases the performance of the method. The blue color channel was chosen by experiments with a validation set. The resulting distribution for color differences follows a Laplacian distribution. **maybe add distribution figure** To include the color distribution into our measurement model, we extend the calculation of the term $p(s_{t,i}|st-1, V)$ what is intuitive because the color is a property of the surface and, to know the color, the point has to be visible in the previous frame:

$$p(s_{t,i}|st-1, V) = p_s(s_{t,i}|st-1, V) p_c(s_{t,i}|st-1, V) \quad (14)$$

where $p_s(s_{t,i}|st-1, V)$ is the probability for the spatial matching as before and $p_c(s_{t,i}|st-1, V)$ is the probability for the color match. For the term $p_c(s_{t,i}|st-1, V)$ it does not suffice just to use the learned color model. This is due to changes in lighting, lens flare, and other cases that can change the observed colors significantly. Therefore, we need to introduce a probability $p(\neg C)$ for cases where the learned color model can not be applied. Now we can refine the probability for a color match:

$$\begin{aligned}p_c(s_{t,i}|st-1, V) &= p(C) p_c(s_{t,i}|s_{t-1}, V, C) + \\ &\quad p(\neg C) p_c(s_{t,i}|s_{t-1}, V, \neg C)\end{aligned}$$

$p_c(s_{t,i}|s_{t-1}, V, C)$ is the color distribution learned from the training set. $p_c(s_{t,i}|s_{t-1}, V, \neg C)$ is the probability for a point having any color that does not match the color in the previous frame. Because we use 256 color intensities and we assume for simplicity that the colors are uniformly distributed, we can use $p_c(s_{t,i}|s_{t-1}, V, \neg C) = \frac{1}{255}$.

The probability $p(C)$ that the color of two corresponding points in successive frames should match could be trained again. Though, there is a problem with the resolution of the sample in the annealed dynamic histogram. For coarse resolutions, the likelihood of a color matching is smaller than for good resolutions. Therefore, we can model $p(C)$ as function of the sampling resolution:

$$p(C) = p_c \exp\left(\frac{-r^2}{2\sigma_c^2}\right) \quad (15)$$

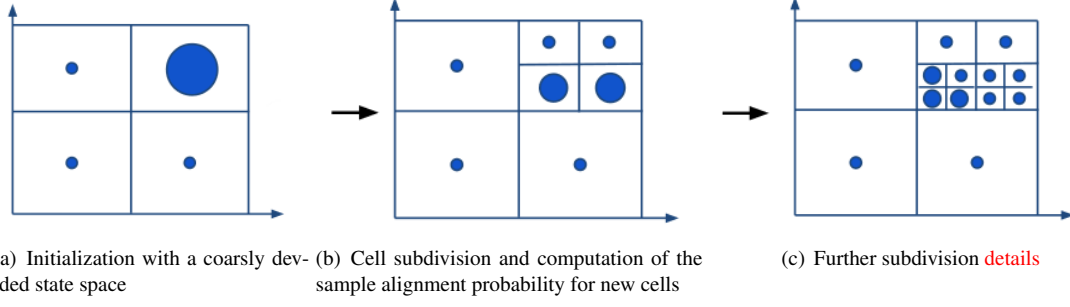


Figure 6: Dynamic refinement of an annealed dynamic histogram. The grid cells divide the state space. The size of the circles indicates the probability for the state in the cell given the measurements [HLTS14].

with sampling resolution r (as interval size, not as number of intervals), parameter p_c for the probability with ideal resolution $r = 0$, and parameter σ_c which defines how fast $p(C)$ decreases with increasing resolution. Now we can revise measurement probability by using the color probability

$$p_c(z_{t,i}|x_t, z_{t-1}, V) = p(C)p_c(z_{t,i}|\text{ccp}(z_{t,i}), V, C) + p(\neg C)p_c(z_{t,i}|\text{ccp}(z_{t,i}), V, \neg C) \quad (16)$$

what results in

$$p(z_t|x_t, z_{t-1}) = \eta \left(\prod_{z_{t,i} \in \mathcal{Z}_t} p_s(z_{t,i}|x_t, z_{t-1}) p_c(z_{t,i}|x_t, z_{t-1}, V) + k_3(k_4 - p_s(z_{t,i}|x_t, z_{t-1})) \right). \quad (17)$$

with $k_3 = k/(k+1)$, where k is from Equation 13, and the smoothing parameter k_4 that has to be found by training.

3.3 Annealed Dynamic Histograms

With the measurement model we have derived up to now, the probability for the current measurement given an assumed state can be computed. To search the state space for the state that is most likely given the measurement, we use an *annealed dynamic histogram* [HLTS14]. We use a histogram because it allow to globally search the state space, in contrast to ICP, and to have multiple hypothesis. The histogram divides the state space into grid cells. For each of these grid cells we compute the probability $p(x_t|z_1, \dots, z_t)$. In an ordinary histogram, it would be necessary to densely sample the state space to get a precise result. This would be computationally costly and prevents the use in a system with real-time requirements. Therefore, we use a dynamic histogram where only the areas with a high probability are densely sampled. Subsection 3.3.1 describes how the annealed dynamic histogram is initialized with a coarse resolution and is then dynamically refined to increase the density in the important areas. Though, the coarse resolution and the dynamically change of it have the drawback that in the areas with coarse resolution the measurements are less likely to fit than in the densely sampled areas. How this problem is solved by considering the resolution of a grid cell in the measurement model is presented in Subsection 3.3.2. How the tracking estimate can be returned as result is shown in Subsection 3.3.3.

3.3.1 Dynamical Refinement

To build the annealed dynamic histogram, we start with a coarsely divided state space and compute the sample alignment probability $p(x_t|z_1, \dots, z_t)$ for each cell. Figure 6(a) shows an example initialization. Then a cell is chosen to be divided into k subcells as in Figure 6(b) and 6(c). For the new created cells, the sample alignment probability is computed again. To compute the probabilities for the new subcells, we first define $|c|$ as the volume of cell c and R as the region of cell we chose to subdivide into subcells c_i . This

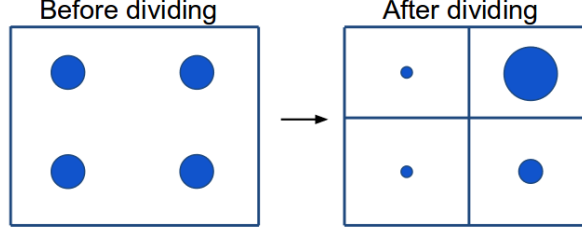


Figure 7: Before deviding a parent-cell we assume that its probability is equally distributed among the k subcells. After deviding, each subcell has its own probability. [HLTS14].

region does not have to be contiguous. The new probability $p(c_i)$ of subcell c_i can be computed as follows:

$$\begin{aligned}
 p(c_i) &= p(c_i \cap R) \\
 &= p(c_i | R) p(R) \\
 &= \frac{p(x_i | z_1, \dots, z_t) |c_i|}{\sum_{c_j \in R} p(x_j | z_1, \dots, z_t) |c_{j \text{ notiright?}}|} p(R) \\
 &= \eta p(x_i | z_1, \dots, z_t) p(R)
 \end{aligned} \tag{18}$$

Thus, the intuitive property $\sum_{c_i \in R} p(c_i) = p(R)$ holds. η is again used for normalization and depends only on the the subcells in region R . Therefore, the probabilities of all cells outside of R are not changed.

Loosely speaking, the criteria that chooses which cells to devide in the next step, tries to maximize the information gain. Prefered subdivisions result in a more definite distribution of probabilities in the subcells. In other words, the probability of the cell to devide is condensed in a few subcells instead of uniformly distributed. To measure this information gain, we inspect the distribution in the possible subcells before and after deviding. Let distribution B be currently estimated distribution in the subcells before deviding. Because we only know the probability of the parent-cell, we assume that this probability is equally distributed among the subcells as illustrated in the left of Figure 7. After deviding the parent-cell, each of the k subcell has its own probability and the only constraint is that the sum of the subcell probabilities has to match the parent-cells probability $\sum_{j=1}^k p_j = P_i$. The new distribution of probabilities among the subcells is called A and is a better approximation of the true posterior than B .

This kind of information gain can be computed with the Kullback–Leibler divergence (*KL-divergence*) [Kul97]. The KL-divergence of B from A measures the information loss when A is approximated with B . In our case, we can compute the KL-divergence with

$$D_{KL}(A||B) = \sum_{j=1}^k p_j \ln \left(\frac{p_j}{P_i/k} \right) \tag{19}$$

where A and B are the distributions after and before deviding as described before. In the mostly preferred case of a subdivision, $p_{j'} = P_i$ for one j' and $p_j = 0$ for all $j \neq j'$. This is also the case in which the KL-divergence has its maximum value

$$D_{KL}(A||B) = P_i \ln(k). \tag{20}$$

The minimum value of the KL-divergence $D_{KL}(A||B) = 0$ is reached when the probability P_i of the parent-cell is uniformly devided among the subcells. This is truly the minimum value because the KL-divergence is always non-negative [Kul97] and in this case there is no profit in deviding this parent-cell. With Equation 20 we can derive that the maximum KL-divergence per second is $P_i \frac{\ln(k)}{kt}$ where t is the time to compute a probability for a subcell with the measurement model. Because k is constant and t should roughly be the same over the whole state spave, we have to devide the cells with the highest probability first to convert as fast as possible to the true posterior. If we want to devide all cells that have a higher probability than a threshold p_{min} , we can also devide all these cells in each iteration, as it is done in Figure 6. This also

yields a simple termination criteria. To maximize the the convergence speed to the true posterior, k should be chosen as small as possible. For example if the histogram has d dimensions, $k = 3^d$ could be used.

3.3.2 Annealing

With the devision of cells into k subcells and the criteria to choose which cells to devide, we have a dynamic histogram that works in principle. Because of the coarse resolution of the histogram, especially at the initialization, we can not expect to find a good alignment between the two point clouds in the current and previous frame. The coarse resolution thus introduces an additional error-source in the method. A solution for this problem is to include the error resulting from the resolution as variance into the measurement model. We increase the variance of the measurement model Gaussian by a value Σ_g . Because the introduced error is expected to be smaller for a better resolution, Σ_g is expressed as a function proportional to the resolution in the currently inspected cell. The updated variance of the measurement model then is $\Sigma = 2\Sigma_e + \Sigma_r + \Sigma_g$. As the resolution improves, the term for Σ_g decreases towards 0 and the variance converges against the value as before. Therefore, the measurement model is annealed as the resolution is improved.

3.3.3 Resulting Tracking Estimate

After terminating because all cell-probabilities are below the threshold p_{min} or the computation was stopped due to real-time restrictions, the result of the position and velocity estimation can be returned. There are multiple possibilities what result can be returned by the histogram. The simplest approach would be to return the mean and variance of the distribution. An alternative would be to return the mode of the distribution. For sophisticated planners which would be used in an autonomous car, also the complete probability distrubution as a density tree could be returned [TFBD01]. Using the mean of the distribution has the advantage that this would minimize the *Root-Mean-Square error (RMS error)* as shown in [HLTS14]. **Probably show this?**

4 Evaluation

This section evaluates the tracker using the position and velocity estimation with annealed dynamic histograms and a model which combines cues from 3D shape, color, and motion. It presents the experiments and results of [HLTS14]. The main criteria of the evaluation are the robustness, the precision, and the runtime of the proposed method. The performance in these criteria is compared with other widely used tracking methods for position and velocity estimation, such as ICP and Kalman filters.

Although there are some existing evaluation methods for tracking, they mostly are not applicable or not suitable for the autonomous driving application. Many standard evaluation techniques are not applicable because the method we want to evaluate only focuses on a subpart of tracking, namely position and velocity estimation. From the tracking evaluation techniques for tracking multiple objects, the metric called *multiple object tracking accuracy (MOTA)* can not be used because it incorporates penailties for wrong assignments called id switches. *Multiple object detection accuracy (MODA)* considers the amount of incorrect detections (e.g. false positives). *Multiple object detection precision (MODP)* measures the position detection in single frames (e.g. to find the centroid). These three metrics are not aplicable here, because the presented method is not responsible for these problems. The metric called *multiple object tracking precision (MOTP)* would be suitable for the method because it only evaluates the precision of the position estimation given a correct matching [KR08, SN07]. However, the authors of the presented paper focus on measuring the *Root-Mean-Square error (RMS error)*

$$e_{RMS} = \sqrt{\mathbb{E}((\hat{v}_t - v_t)^2)} \quad (21)$$

where \mathbb{E} is the mean and $\hat{v}_t - v_t$ is the velocity tracking error. We focus here on the velocity instead of the whole state with position and velocity because the position $x_{t,p}$ in the state is relative to the objects position in the previous frame and mainly used for estimating the velocity with the motion model. The absolute position of the tracked object can easily be computed as the centroid of the point cloud and thus has not to be evaluated here. The RMS error is widely used and has the property to give large errors a higher influence

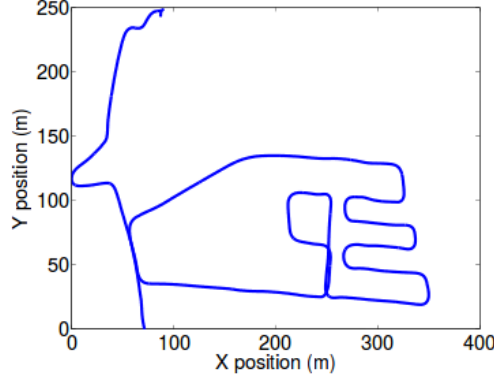


Figure 8: Path taken by the tracking car on the parking space [HLTS14].

than many small ones have. A problem with the RMS error, which was not mentioned by the authors of the paper, is that it is independent of the distance to the object. Intuitively, the tracking error for distant objects would be higher than for close objects because the point clouds have less measurement points. However, the authors might have considered it in the evaluation because the distance to the tracked object is incorporated in the variance of the measurement model Gaussian and therefore also in the variance of the returned tracking estimate.

To properly evaluate the performance of the tracker, a large dataset with many different objects to track is needed, because in practise an autonomous car has to track many different objects with different shapes, color distributions, and motion patterns. Therefore, the acquisition of evaluation data has to be scalable. This excludes methods as done by [MLvHW11] where the tracking and tracked cars were equipped with additional sensors to measure the positions and velocities. The authors of the paper presented in this report propose two approaches to automatically generate test data and evaluate the tracking with it. In both approaches, the car was driven around and the sensor data with object detection and object assignment was recorded. Therefore, a large amount and variety of tracked object in the surrounding of the car is automatically recorded and the data is taken from an environment that is close or equal to the application environment. In the first approach which is presented in Subsection 4.1, the car drives in a parking space where the tracked objects are not moving. By assuming that the car is standing still, the tracked objects seem to be moving and their velocity can be tracked. The results can be compared to the velocity calculated with the car's movement and the distance to the tracked object. The second approach is described in Subsection 4.2 and utilizes a recorded dataset from the car driving in real traffic. Using the relative positions of the point clouds calculated by the tracker, the point clouds can be merged to build a model of the tracked object. Then a metric is introduced to measure the quality of the build model.

Before the tracking can be evaluated, the various parameters introduced in the method have to be determined. This was done by using a training dataset that is different from the test sets used later. The training dataset was generated by recording while the car drives past parked cars. The approach is similar to the first evaluation approach. The most important parameters determined in [HLTS14] are the initial coarse resolution of 1m for the annealed dynamic histogram, the variance $\Sigma_g = gI$ to anneal the measurement model, where g is the cell resolution and I is the identity matrix, and $p_c = 0.05$ for the color model. This results in a low probability $p(C)$ for a color match because of many underexposed frames and frames with lense flare.

4.1 Relative Reference Frame

In the first approach, the test data is recorded by a car driving on a parking space. During the recording of 6.6 minutes, about 560 cars were tracked. This large dataset allows a good quantitative evaluation. The objects were tracked in a local reference frame. This means that the tracker assumes that the recording car stands still and the tracked objects move around it. The path of the car through the parking space is shown in Figure 8. Even in this simplified scenario, many real world challenges for the tracking are

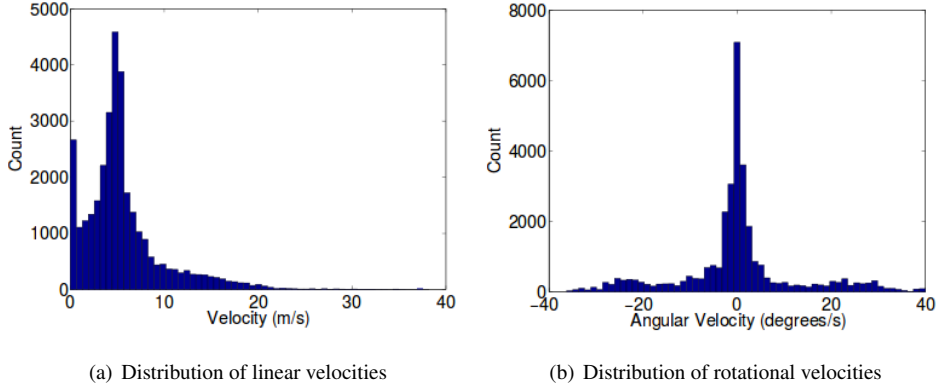


Figure 9: Distribution of the ground-truth velocities of the tracked objects in the local reference frame [HLTS14].

present in the dataset. Viewpoint changes, changes in occlusion and color changes due to reflections from different viewpoints are similar to driving in traffic. During the recording, the linear and rotational velocity of the tracking car is logged. With this information, the ground-truth velocity of the tracked objects can be computed. When the car is driving just forward this is easy. When the car is turning, the relative position of the tracked objects is used additionally. Because of many objects being inside and outside the turning circle of the car, the distribution of velocities of the tracked objects is wider than the simple velocity distribution of the car. These velocity distributions are plotted in Figure 9(a) and 9(b).

To evaluate only the position and velocity estimation part of the tracking pipeline, some tracked objects over a number of successive frames, called tracks, are filtered out. About 7% of the tracks were filtered out due to undersegmentation issues. Undersegmentation occurs when multiple nearby objects are not distinguished in the segmentation step and therefore wrongly detected as one object. These tracks are filtered out because of the ambiguity in the ground-truth velocity. Tracks with oversegmentation, where one object is split into multiple peaces is not filtered out.

We now compare the performance of the proposed tracking method with several widely used baseline methods. One the one hand, we compare the RMS error and on the other hand the mean runtime. Figure 10 shows the results of the comparison. Plotted are RMS errors at different mean runtimes for the method presented in this report as well as four other baseline methods.

The first baseline method we use for comparison is a Kalman filter that uses only the centroid of point cloud in a frame in its measurement model. This method is widely used because of the easy implementation and the fast computation. As shown in Figure 10 the Kalman filter is extremely fast with a computational time below 0.1 milliseconds. This was expected because the Kalman filter only uses the centroid instead of aligning two point clouds. The RMS error is 0.78 m/s and shows that the Kalman filter is not very accurate. For the Kalman filter, there is only a single mean runtime because the Kalman filter only has a single computation step and no dynamic improvement steps.

Furthermore, we analyze the performance of ICP in different variants. These variants differ in the initialization of ICP and wheather they are used as a measurement model in for Kalman filter. The basic point-to-point ICP algorithm is described in [RC11] and uses the centroid of the point clouds to align as initialization. The algorithm was run with up to 100 incremental alignment iterations. The RMS error with different mean runtimes is shown in Figure 10 and is about 1 m/s. This is 23% worse than the RMS error of a simple Kalman filter and therefore no good tracking performance. This bad performance in comparison to the Kalman filter is caused by the missing motion model which is important for robust tracking. Without a motion model, only the last two frames can be used to estimate the velocity of the tracked object. Therefore, a single incorrect alignment as, for example, show in Figure 3 significantly impacts the tracking error. A Kalman filter with its motion model can refine the result of many more previous alignments into one Gaussian distribution and can compensate wrong alignments because the ceartainty of a measurement can be considered as variance when feeding the measurement into the Kalman filter.

By combining the Kalman filter and ICP into one method, the drawbacks of both methods can be removed.

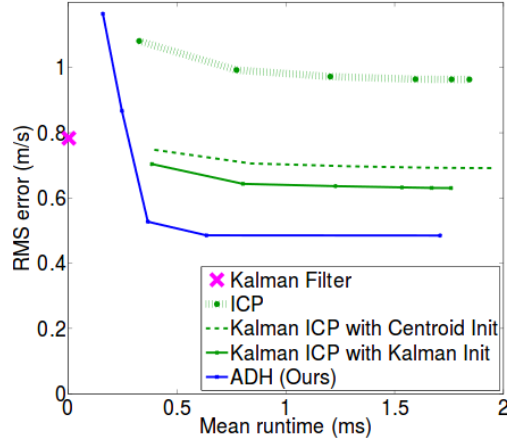


Figure 10: Comparison of the proposed method with annealed dynamic histograms with other baseline methods. Plotted is the RMS error for different runtimes of the algorithm [HLTS14].

ICP can be used as measurement model to align the point clouds in successive frames what removes the information loss in the basic Kalman filter that only uses the centroid. The result can then be used in the motion model of the Kalman filter what increases the robustness against failures of ICP. As initialization either the alignment of the centroids is used or the result of the Kalman filter that uses the centroids as described before.

The performances of the ICP variants with a Kalman filter as motion model is shown in Figure 10. The variant with centroid initialization performs 11.7% better than the simple Kalman filter thus much better than the basic ICP algorithm without a motion model. If the initial alignment is computed by a first Kalman filter, we achieve the best performance of all baseline variants with an RMS error of 0.63 m/s. The method presented in this report achieves with 0.43 m/s a lower RMS error than all baseline methods. It is more robust than ICP because it does not depend on a good initialization what is due to the global search of the annealed dynamic histogram. **at the same time faster, only kalman faster but..., accuracy-distance, color improvement**

4.2 Model Crispness

5 Conclusion

References

- [AA12] Asma Azim and Olivier Aycard. Detection, classification and tracking of moving objects in a 3D environment. In *Intelligent Vehicles Symposium (IV), 2012 IEEE*, pages 802–807. IEEE, 2012.
- [Ack13] Evan Ackerman. Amazon Promises Package Delivery By Drone: Is It for Real? <http://spectrum.ieee.org/automaton/robotics/aerial-robots/when-drone-delivery-makes-sense>, 2013.
- [DRU08] Michael Darms, Paul Rybski, and Chris Urmson. Classification and Tracking of Dynamic Objects with Multiple Sensors for Autonomous Driving in Urban Environments. In *Intelligent Vehicles Symposium, 2008 IEEE*, pages 1197–1202. IEEE, 2008.
- [ECM04] Vladimir Estivill-Castro and Blair McKenzie. Hierarchical Monte-Carlo Localization Balances Precision and Speed. In *Australasian Conference on Robotics and Automation*, 2004.

- [Eur15] European Commission / Directorate General Energy and Transport. Road safety evolution in EU. http://ec.europa.eu/transport/road_safety/pdf/observatory/historical_evol.pdf, 2015.
- [FHB12] Adam Feldman, Maria Hybinette, and Tucker Balch. The Multi-Iterative Closest Point Tracker: An Online Algorithm for Tracking Multiple Interacting Targets. *Journal of Field Robotics*, 29(2):258–276, 2012.
- [Gui08] Erico Guizzo. Three Engineers, Hundreds of Robots, One Warehouse. *Spectrum, IEEE*, 45(7):26–34, 2008.
- [HLT13] David Held, Jesse Levinson, and Sebastian Thrun. Precision Tracking with Sparse 3D and Dense Color 2D Data. In *Robotics and Automation (ICRA), 2013 IEEE International Conference on*, pages 1138–1145. IEEE, 2013.
- [HLTS14] David Held, Jesse Levinson, Sebastian Thrun, and Silvio Savarese. Combining 3D Shape, Color, and Motion for Robust Anytime Tracking. In *Proceedings of Robotics: Science and Systems*, Berkeley, USA, July 2014.
- [HLTS15] David Held, Jesse Levinson, Sebastian Thrun, and Silvio Savarese. Anytime Tracking. http://stanford.edu/~davidheld/DavidHeld_files/RSS2014_Poster.pdf, 2015.
- [IRdSvdZ12] Luca Iocchi, Javier Ruiz-del Solar, and Tijn van der Zant. Domestic Service Robots in the Real World. *Journal of Intelligent & Robotic Systems*, 66(1):183–186, 2012.
- [KH95] James J Kuch and Thomas S Huang. Vision Based Hand Modeling and Tracking for Virtual Teleconferencing and Telecollaboration. In *Computer Vision, 1995. Proceedings., Fifth International Conference on*, pages 666–671. IEEE, 1995.
- [KMPS12] Ralf Kaestner, Jérôme Maye, Yves Pilat, and Roland Siegwart. Generative object detection and tracking in 3D range data. In *Robotics and Automation (ICRA), 2012 IEEE International Conference on*, pages 3075–3081. IEEE, 2012.
- [KR08] Bernardin Keni and Stiefelhagen Rainer. Evaluating Multiple Object Tracking Performance: The CLEAR MOT Metrics. *EURASIP Journal on Image and Video Processing*, 2008, 2008.
- [Kul97] Solomon Kullback. *Information theory and statistics*. Courier Corporation, 1997.
- [LAB⁺11] Jesse Levinson, Jake Askeland, Jan Becker, Jennifer Dolson, David Held, Soeren Kammel, J Zico Kolter, Dirk Langer, Oliver Pink, Vaughan Pratt, et al. Towards fully autonomous driving: Systems and algorithms. In *Intelligent Vehicles Symposium (IV), 2011 IEEE*, pages 163–168. IEEE, 2011.
- [LHT⁺08] John Leonard, Jonathan How, Seth Teller, Mitch Berger, Stefan Campbell, Gaston Fiore, Luke Fletcher, Emilio Frazzoli, Albert Huang, Sertac Karaman, et al. A perception-driven autonomous urban vehicle. *Journal of Field Robotics*, 25(10):727–774, 2008.
- [Mar10] John Markoff. Google Cars Drive Themselves, in Traffic. *New York Times*, 9, 2010.
- [ML12] Dennis Mitzel and Bastian Leibe. *Taking Mobile Multi-Object Tracking to the Next Level: People, Unknown Objects, and Carried Items*. Springer, 2012.
- [MLvHW11] Michael Manz, Thorsten Luetzel, Felix von Hundelshausen, and H-J Wuensche. Monocular Model-Based 3D Vehicle Tracking for Autonomous Vehicles in Unstructured Environment. In *Robotics and Automation (ICRA), 2011 IEEE International Conference on*, pages 2465–2471. IEEE, 2011.
- [MS13] Frank Moosmann and Christoph Stiller. Joint Self-Localization and Tracking of Generic Objects in 3D Range Data. In *Robotics and Automation (ICRA), 2013 IEEE International Conference on*, pages 1146–1152. IEEE, 2013.

- [MSM02] R Marcello, Domenico G Sorrenti, and Fabio M Marchese. A robot localization method based on Evidence Accumulation and Multi-Resolution. In *Intelligent Robots and Systems, 2002. IEEE/RSJ International Conference on*, volume 1, pages 415–420. IEEE, 2002.
- [Ols09] Edwin B Olson. Real-Time Correlative Scan Matching. In *Robotics and Automation, 2009. ICRA'09. IEEE International Conference on*, pages 4387–4393. IEEE, 2009.
- [PT09] Anna Petrovskaya and Sebastian Thrun. Model based vehicle detection and tracking for autonomous urban driving. *Autonomous Robots*, 26(2-3):123–139, 2009.
- [RAK⁺07] Sivakumar Rathinam, Pedro Almeida, ZuWhan Kim, Steven Jackson, Andrew Tinka, William Grossman, and Raja Sengupta. Autonomous Searching and Tracking of a River using an UAV. In *American Control Conference, 2007. ACC'07*, pages 359–364. IEEE, 2007.
- [RC11] Radu Bogdan Rusu and Steve Cousins. 3D is here: Point Cloud Library (PCL). In *Robotics and Automation (ICRA), 2011 IEEE International Conference on*, pages 1–4. IEEE, 2011.
- [RN13] S. Russell and P. Norvig. *Artificial Intelligence: A Modern Approach*. Always learning. Pearson, 2013.
- [SFD02] Daniel Streller, K Furstenberg, and Klaus Dietmayer. Vehicle and object models for robust tracking in traffic scenes using laser range images. In *Intelligent Transportation Systems, 2002. Proceedings. The IEEE 5th International Conference on*, pages 118–123. IEEE, 2002.
- [SN07] Xuefeng Song and Ram Nevatia. Robust vehicle blob tracking with split/merge handling. In *Multimodal Technologies for Perception of Humans*, pages 216–222. Springer, 2007.
- [TBF05] Sebastian Thrun, Wolfram Burgard, and Dieter Fox. *Probabilistic robotics*. MIT press, 2005.
- [TFBD01] Sebastian Thrun, Dieter Fox, Wolfram Burgard, and Frank Dellaert. Robust Monte Carlo localization for mobile robots. *Artificial intelligence*, 128(1):99–141, 2001.
- [TLT11] Alex Teichman, Jesse Levinson, and Sebastian Thrun. Towards 3D Object Recognition via Classification of Arbitrary Object Tracks. In *Robotics and Automation (ICRA), 2011 IEEE International Conference on*, pages 4034–4041. IEEE, 2011.
- [WH12] Nicolai Wojke and M Haselich. Moving Vehicle Detection and Tracking in Unstructured Environments. In *Robotics and Automation (ICRA), 2012 IEEE International Conference on*, pages 3082–3087. IEEE, 2012.
- [WPN12] Dominic Zeng Wang, Ingmar Posner, and Paul Newman. What Could Move? Finding Cars, Pedestrians and Bicyclists in 3D Laser Data. In *Robotics and Automation (ICRA), 2012 IEEE International Conference on*, pages 4038–4044. IEEE, 2012.